Charles Matz
e-mail: charles.matz@power.alstom.com

Giovanni Cataldi

Wolfgang Kappis

ALSTOM (Switzerland) Ltd.,
Brown Boveri Strasse 7,
CH-5401 Baden, Switzerland

Gerd Mundinger
e-mail: gerd.mundinger@ch.abb.com

Stefan Bischoff
e-mail: stefan.bischoff@linde-kryotechnik.ch

Eivind Helland
e-mail: eivind.helland@zurich.com

ABB Turbosystems Ltd.,
Bruggerstrasse 71a,
CH-5401 Baden, Switzerland

Matthias Ripken
Technische Universität Dresden,
Helmholtzstrasse 14,
D-01062 Dresden, Germany
e-mail: matthias.ripken@power.alstom.com

Prediction of Evaporative Effects Within the Blading of an Industrial Axial Compressor

The results of a compressor flow-analysis code calibration study for estimating the effects of water evaporation within the blade rows of industrial axial compressors are presented. In this study, a mean-line code was chosen for the calibration tool due to its accepted use during preliminary design studies, at which time during the compressor design process one would logically consider power augmentation through wet compression. The calibrated code features a nonequilibrium thermodynamic single-droplet evaporation model augmented with an empirical splashing model, which, as input, uses measurements of droplet spectra data taken on water injection nozzles in an intake rig configured with realistic length scales. In addition, a wetted-airfoil-surface flow-angle deviation model is applied to predict changes in compressor stage characteristics, which, in turn, affect the inlet mass flow of the compressor. The test vehicle for calibration was a 50 Hz Alstom industrial gas turbine. Once calibrated, the code was successfully utilized to predict wet-compression effects for three additional like-family Alstom gas turbines operating at constant speed while under full load. The effects modeled by the code include bleed supply pressure suck-down and bleed temperature cool-down effects, as well as compressor inlet mass flow and power consumption effects. [DOI: 10.1115/1.3149285]

Keywords: wet compression, gas turbine, compressor mean-line model, nonequilibrium thermodynamics, multiphase flow, interphase slip, surface film, droplet spectrum, droplet splashing, airfoil flow-angle deviation

1 Introduction

The injection of water into compressors has been the subject of research for many years. Prompted initially by either concerns about rain and ice ingestion in aircraft jet engines, or by the temporary thrust increase achievable in aircraft engines by intentionally injecting water during take-off, attention then also focused on the potential for power augmentation by water injection into land-based industrial gas turbines.

In the early 1960s, Hill [1] investigated the axial compressor performance with water injection on two turboshaft engines. He determined that the injection of water tends to cause an aerodynamic load shift to the rear stages of a compressor and a subsequent mass flow increase consistent with aerodynamically unloaded front stages. In addition, he theorized that the bulk of evaporation occurs within wall films as opposed to within the air stream. He arrived at such a conclusion based on calculations of evaporation rates within fully developed turbulent boundary layers covering the surface areas he assumed wetted, mainly the compressor gas path outer diameter and the pressure surfaces of the airfoils.

In the 1980s an investigation was carried out at the Purdue University motivated by instances in which water is unavoidably ingested into aircraft jet engines during rainstorms, or due to tire-generated spray from flooded runway surfaces [2]. Unlike the Hill study [1], this investigation observed a reduction in compressor mass flow. It should be pointed out, however, that droplet sizes were relatively large—two mean droplet sizes were injected, 90 and 600 μm. Moreover, the lowest injection rate tested was 2% of air mass flow, roughly twice the level normally injected into industrial compressors.

Interest in water injection into industrial compressors intensified in the late 1990s as power generation with gas turbines increased significantly throughout the world. For that matter, Utamura et al. [3] showed that water droplet size strongly affects evaporation rates within a compressor gas path. They made predictions regarding the stagewise penetration of water, which they confirmed via experimentation. Responding to the Utamura paper [3], Horlock [4] revisited an earlier work in which he cooperated with Camp [5] in determining the magnitudes of compressor stage off-design effects with water evaporation. The Utamura paper [3] led him to believe that he underestimated these effects, and his subsequent work accounted for the effects of the evaporation of injected water prior to reaching the face of the compressor in an industrial gas turbine.

In 2001, Zhluktov et al. [6] published a study aimed at generating compressor performance maps with water injection. In it, they build myriad two-phase-flow effects into a compressor mean-line model, including centrifugal, Coriolis, and drag forces acting on the droplets, evaporation within films formed on the airfoils and on the casing, as well as the splashing of the droplets.

White and Meacock [7] took a more simplified approach to compressor mean-line modeling with water injection in their 2003 work, their argument being that droplet sizes large enough to necessitate the modeling of centrifugal effects and splashing interactions would prove to be too large for industrial gas turbine application, since the horsepower required to drive the compressor would increase due to the disruption of the flow field by airfoil and casing surface films, in effect, partially negating the beneficial

Contributed by the International Gas Turbine Institute of ASME for publication in the JOURNAL OF TURBOMACHINERY. Manuscript received October 19, 2008; final manuscript received November 3, 2008; published online May 5, 2010. Review conducted by David Wisler. Paper presented at the ASME Turbo Expo 2008: Land, Sea and Air (GT2008), Berlin, Germany, June 9–13, 2008.

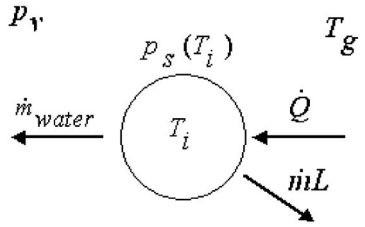

Fig. 1 Evaporating droplet depicting heat and mass fluxes

thermodynamic effects from intracompressor cooling. In addition, they argued that airfoil erosion levels associated with such large droplets would be prohibitive due to blade lifetime concerns. Alternatively, they considered the use of superheated feed water—a relatively new technology described by van Liere et al. [8], in which the injected droplets burst into tiny droplets of the order of 2 μm upon making contact with the cooler air of a gas turbine intake manifold—to be the only practical method for compressor gas turbine power augmentation via water injection.

In wet cascade experiments, Day et al. [9] were able to separate mechanical torque effects from airfoil flow-angle deviation effects. Such is crucial to any modeling of wet-compression effects since airfoil deviation influences compressor stage characteristics, and thus plays a pivotal role in the stagewise work redistribution of industrial axial compressors with water injection.

Most recently, Meacock and White [10] published an advancement to their earlier work, in which they discussed mean-line-generated compressor maps for multispool industrial gas turbines derived from aeroengines. Their conclusions are similar for multispool machines as they are for single-spool machines. Mainly, compressor air mass flow increases, and work shifts aft, just as Hill [1] observed some 40 years earlier.

This work focuses on the mean-line modeling of evaporative effects in compressors of Alstom 50 Hz and 60 Hz industrial gas turbines equipped with water injection systems, which produce droplets of mean Sauter diameter within the 20–25 μm range. Section 1 describes a single-droplet nonequilibrium evaporation model. Discussion then focuses on a droplet-splashing model superimposed on the single-droplet model motivated by the need for better prediction of interstage compressor bleed supply pressure effects with increasing water injection rates. Next, discrepancies in compressor air mass flow effects with water injection are explained by the addition of a wetted-airfoil-surface flow-angle deviation model. Finally, code calibration results are presented, with particular attention on compressor mass flow effects from test runs made at two different ambient humidity levels on two different 50 Hz units equipped with identical compressor models.

2 Single-Droplet Evaporation Model

The evaporation logic built into the compressor mean-line is essentially the gas-droplet evaporation model of Young [11], in which the diffusion of the evaporated vapor into the surrounding gas is driven by the difference in vapor pressure between the gas and the droplet surface. The calculation is not a true two-phase calculation. That is, the gas is considered to be a continuum, which is not affected by droplet evaporation during the solving of the heat transfer equations; i.e., the velocity, temperature, and vapor pressure of the gas are held constant during droplet evaporation. The droplets are modeled as uniform-temperature spheres, which do not interact with one another; see Fig. 1. The forces acting on the droplets are assumed to be dominated by drag; i.e., contributions due to virtual mass, pressure gradient, Basset term, and gravity are neglected. Due to the fact that all calculations take place on the RMS streamline of a compressor mean-line code, no radial slinging of droplets is possible. Finally, interphase slip occurs in the meridional coordinate only, the tangential direction being neglected.

2.1 Interphase Transfer of Mass, Momentum, and Heat. For a single droplet identified by class i, with diameter D_i, temperature T_i, and meridional velocity $c_{m,i}$, it follows

$$\frac{dD_i}{dt} = -F_m \frac{4}{D_i}\frac{\rho_g}{\rho_i}\Gamma \ln\frac{p_g - p_v}{p_g - p_s(T_i)} \tag{1}$$

$$\frac{dT_i}{dt} = F_h 6N_u \frac{\lambda(T_g - T_i)}{D_i^2 \rho_i c_{p,i}} + 3\frac{L_i}{c_{p,i}}\frac{1}{D_i}\frac{dD_i}{dt} \tag{2}$$

and

$$\frac{dc_{m,i}}{dt} = \frac{3}{4}\frac{\rho_g}{\rho_i}\frac{1}{D_i}|c_{m,g} - c_{m,i}|(c_{m,g} - c_{m,i})c_{D,i}(\mathrm{Re}_i) \tag{3}$$

where L is the specific enthalpy of evaporation of the droplet, λ is the thermal conductivity, Γ is the diffusion coefficient, and c_D is the drag coefficient. The Reynolds number is defined by

$$\mathrm{Re}_i = \frac{D_i|c_{m,g} - c_{m,i}|\rho_g}{\mu_g} \tag{4}$$

The correlation used for the drag coefficient of a droplet is defined by

$$c_{D,i} = 0.36 + 5.48\ \mathrm{Re}_i^{-0.573} + 24/\mathrm{Re}_i \tag{5}$$

The empirical correction factors F_m and F_h take into account the increased mass and heat transfer due to convective effects, and are functions of the Reynolds, Schmidt, and Prandtl numbers

$$F_m = 1 + 0.276\ \mathrm{Re}_i^{1/2}\ \mathrm{Sc}^{1/3} \tag{6}$$

$$F_h = 1 + 0.276\ \mathrm{Re}_i^{1/2}\ \mathrm{Pr}^{1/3} \tag{7}$$

In the case of $T_i < T_g$, heat is transported into the droplet via heat conduction. After reaching a stationary droplet temperature, this heat is compensated for by the latent heat of evaporation ($dT_i/dt \to 0$). For constant droplet temperature and constant state of the gas, it follows

$$\frac{dD_i^2}{dt} = -F_m \frac{8}{D_i}\frac{\rho_g}{\rho_i}\Gamma \ln\frac{p_g - p_v}{p_g - p_s(T_i)} = \mathrm{const} \tag{8}$$

Hence,

$$D_i \propto \sqrt{t} \tag{9}$$

The meridional coordinate s of the droplet follows from

$$\frac{ds}{dt} = c_{m,i} \tag{10}$$

For a droplet class, i, the number of droplets per unit of time, $\dot{n}_i$, in the stream surface is related to the droplet mass flow, $\dot{m}_i$, by

$$\dot{m}_i = \dot{n}_i \rho_i \frac{\pi}{6} D_i^3 \tag{11}$$

Hence, the number of droplets per unit time $\dot{n}_i$ is assumed constant; i.e., droplet coalescence, disintegration, and nucleation are not taken into account.

2.2 Validation of Single-Droplet Model. This single-droplet evaporation model was validated using an experiment by Kobayasi [12], in which water droplets were evaporated in dry, quiescent air heated by an electric furnace. Interphase slip was made vanishingly small by setting both the droplet and flow velocities to 1 m/s; see Fig. 2 for the first attempt obtained from modeling a droplet of initial diameter 1.38 mm and initial temperature of 293 K. The droplet quickly reaches a temperature of about 314 K, indicating that the precise value of the initial droplet temperature is not that important. Also of note, the decrease in droplet diameter goes roughly with the square root of the temperature. Note that the evaporation time predicted is about 30% longer than mea-

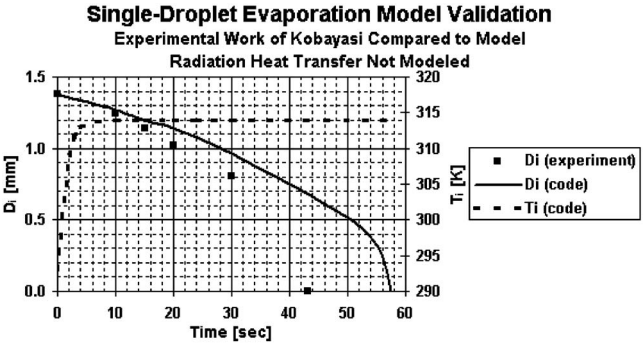

Fig. 2 Single-droplet model first attempt: No radiation heat transfer from walls of the electric furnace modeled

sured in the experiment.

The faster evaporation in the experiment is due to radiative heat transfer from the walls of the electric furnace. Assuming that the droplet is surrounded by black walls of temperature T_{wall}, the heat flux due to radiation is

$$\dot{Q}_{\text{rad}} = \varepsilon \pi D_i^2 \sigma (T_{\text{wall}}^4 - T_i^4) \tag{12}$$

where the Stefan–Boltzmann constant

$$\sigma = 5.67 \times 10^{-8} \ \text{W/m}^2\,\text{K}^4 \tag{13}$$

The Nusselt number Nu is defined by

$$\text{Nu} = \frac{2Z}{\exp(Z) - 1} \tag{14}$$

where

$$Z = \frac{c_{pv}\rho_i}{4\lambda} D_i \frac{dD_i}{dt} \tag{15}$$

From the ratio of radiative to conductive heat flux

$$\frac{\dot{Q}_{\text{rad}}}{\dot{Q}_{\text{cond}}} = \frac{D_i \varepsilon \sigma (T_{\text{wall}}^4 - T_i^4)}{Nu\lambda(T_g - T_i)} \tag{16}$$

it follows that the influence of radiative heat transfer increases proportional to droplet size. Taking radiative heat transfer into account in the interphase heat transfer equation, the following may de derived:

$$\frac{dT_i}{dt} = F_h 6 \ \text{Nu} \frac{\lambda(T_g - T_i)}{D_i^2 \rho_i c_{p,i}} + 6\frac{\varepsilon\sigma(T_g^4 - T_i^4)}{D_i \rho_i c_{p,i}} + 3\frac{L}{c_{p,i}}\frac{1}{D_i}\frac{dD_i}{dt} \tag{17}$$

where the wall temperature is approximated by the gas temperature, and the emissivity ε is assumed to be 0.96. As shown in Fig. 3, the inclusion of the effect of the additional radiative heat transfer improves the prediction. Due to radiation, the maximum droplet temperature is increased to about 318 K. Moreover, as the droplet evaporates, the droplet temperature is not independent of droplet size.

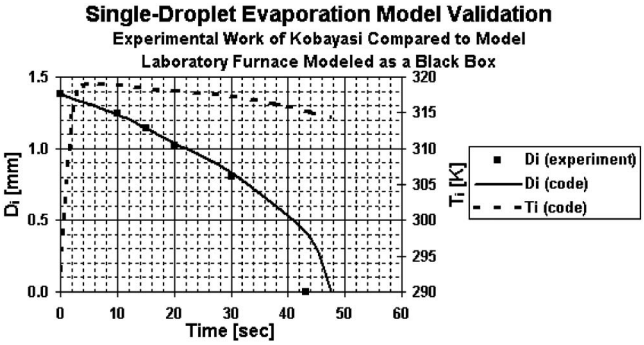

Fig. 3 Single-droplet model second attempt: Radiation heat transfer from walls of the electric furnace modeled

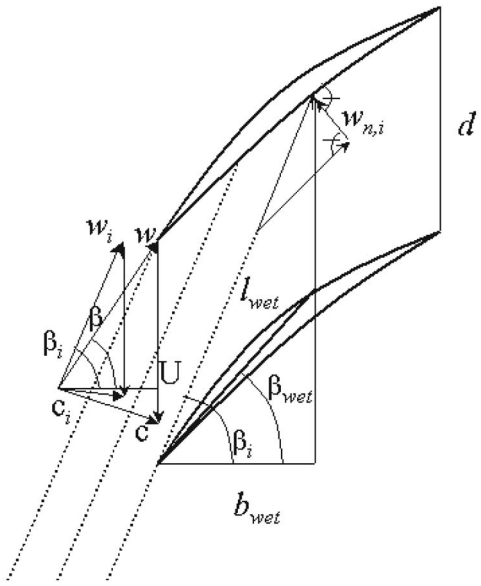

Fig. 4 Inertial effect of droplet of a certain size striking airfoil pressure surface

3 Droplet Splashing-Deposition Model

Water injection tests were performed on Alstom gas turbines beginning in 2001. Consistent with the experiences of Hill and others, the pretest mean-line prediction utilizing the single-droplet evaporation model indicated that compressor work would shift rearward, pulling more mass flow through the compressor and reducing intracompressor bleed supply pressure levels. However, during a test parametric on a 50 Hz unit set at base load, in which stable, constant-speed data points at various water injection rates from roughly 0.25% of engine air mass flow up to 1.1% were obtained, it was noticed that the measured magnitudes of bleed supply pressure suck-down were significantly underpredicted. Hence, the evaporation rate within the compressor blade rows had been calculated to be much slower than reality. For that reason, an enhanced evaporation model was written for the evaporative-cooling compressor mean-line code, which augmented the single-droplet model.

The enhanced evaporation model includes two additional effects. First, an empirical splashing model accounts for tiny secondary droplets returning to the flow field, and in the process significantly increasing the total droplet surface area operated on by the single-droplet evaporation model. Second, a film evaporation model accounts for droplets entering boundary layers with relatively high velocities, which evaporate more rapidly due to enhanced heat transfer. To understand both effects requires that the code estimates impact rates of droplets with blade surfaces.

3.1 Droplet Impact Rate. The droplet impact rate with the airfoil surfaces is estimated using the interphase slip model, which is part of the single-droplet evaporation model previously discussed. As shown in Fig. 4, there exists a limiting axial penetration depth into a blade or vane row, b_{wet}, at which point a water droplet of a particular size is too massive to follow the flow stream, and impacts the surface.

The length of the droplet-impacted surface, l_{wet}, may be approximated by

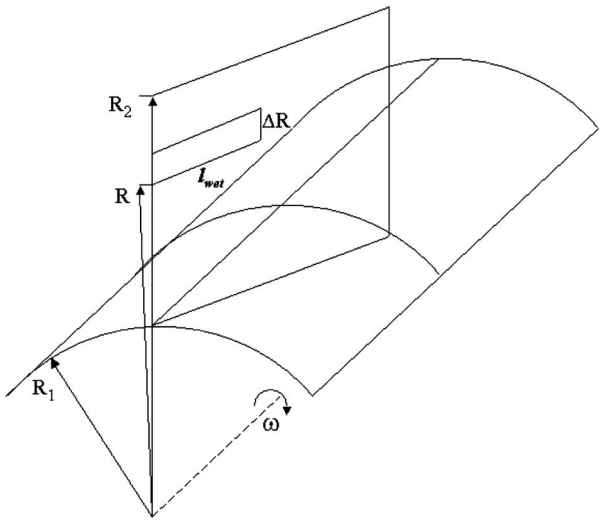

Fig. 5 Differential blade surface element showing droplet impact frequency from a droplet of a certain size

$$l_{\text{wet}} = \frac{b_{\text{wet}}}{\cos \beta_{\text{wet}}} \tag{18}$$

where β_{wet} is a mean blade angle of the droplet-impacted surface; see Fig. 5. For a given relative flow angle β_i of the droplets, it follows from the sine rule that

$$l_{\text{wet}} = d\frac{\sin(90\ \text{deg} - \beta_i)}{\sin(\beta_i - \beta_{\text{wet}})} \tag{19}$$

where d is the pitch of the cascade. The droplet impact velocity normal to the blade is given by

$$w_{n,i} = w_i \sin(\beta_i - \beta_{\text{wet}}) \tag{20}$$

For n_b blades it takes N droplets to cover the blade surface elements of size $l_{\text{wet}}\Delta R$ as follows:

$$N\frac{\pi}{4}D_i^2 = n_b l_{\text{wet}}\Delta R \tag{21}$$

The droplet mass flow hitting the blade surface element is

$$\Delta\dot{m} = \Delta\dot{N}_i\rho_i\frac{\pi}{6}D_i^3 \tag{22}$$

Therefore, the local impact frequency is given by

$$f = \frac{\Delta\dot{N}_i}{N} = \frac{6\Delta\dot{m}_i}{\rho_i\pi D_i^3} = \frac{4n_b l_{\text{wet}}\Delta R}{\pi D_i^2} = \frac{3}{2}\frac{\Delta\dot{m}_i}{\Delta R}\frac{1}{n_b l_{\text{wet}}\rho_i D_i} \tag{23}$$

3.2 Droplet-Wall Interactions. The modeling of droplet-wall interactions requires the estimation of the fractional split between water mass flow that ends up being reflected back into the flow as secondary droplets, and that which deposits on the airfoils as a water film. It is important to point out that for this work the mean-line code has been tuned by two factors in order to match compressor boundary effects—mainly changes in interstage bleed supply pressure—resulting from evaporation within the stages. The first, and more dominant of the two factors, increases the evaporation heat transfer consistent with the increased aggregate droplet surface area due to splashing. The second factor specifies the mass flow fraction of water striking the blades deposited as a film at high Reynolds number. Both tuning factors are reasonable in magnitude based on the study of literature related to the subject.

3.2.1 (Dry) Wall Temperature Regimes. As discussed by Schmehl et al. [13], droplets impacting blade and vane pressure surfaces are subject to various interaction mechanisms, depending on the temperature of the airfoil surface, and by the existence or absence of a liquid film. The behavior a droplet impacting in the absence of a surface film can be characterized by the following three blade surface (wall) temperature regimes:

I. *Cold wall*. Temperatures up to approximately 1.05 times the fluid boiling temperature.
II. *Moderately hot wall*. A transition range up to the modified Leidenfrost temperature.
III. *Hot wall*. Temperatures well above the modified Leidenfrost temperature.

Now, in wet-compression applications of industrial axial compressors, which involve injection rates of the order of 1% of engine mass flow, blade pressure surfaces are assumed covered by films, meaning that one might not think that droplet impacts with dry walls would be of interest. However, as shown in the discussion that follows, the mechanisms of interaction of droplets with blade surfaces covered with water films are similar to those associated with droplets striking dry walls.

3.2.2 Classification of Wall Interactions. For a cold, dry wall, the Reynolds and Laplace numbers are used to derive an expression for the boundary between splashing and deposition. The impact Reynolds number is determined using the normal velocity vector to a blade or vane pressure surface, as discussed in Sec. 3.1,

$$\text{Re}_{\text{imp}} = \frac{w_{n,i}D_i\rho_i}{\mu_i(T_i)} \tag{24}$$

The Laplace number represents the ratio of surface tension of the droplet to momentum transport inside the droplet, and is given by

$$\text{La} = \frac{D_i\rho_i\sigma_i(T_i)}{\mu_i^2(T_i)} \tag{25}$$

In instances of impact with a wall at high Reynolds number—high droplet inertia compared with viscosity—and low Laplace number—low surface tension—the result would be splashing. Conversely, low inertia and high surface tension result in deposition onto the wall. The boundary between splashing and deposition has been determined experimentally by Utamura et al. [3] and is given by

$$S = \frac{\text{Re}_{\text{imp}}}{24\ \text{La}^{0.419}} \tag{26}$$

where $S=1$ corresponds to splashing-deposition boundary, $S>1$ corresponds to the splashing regime, and $S<1$ corresponds to the deposition regime. The fraction of the droplet mass striking a dry wall that is deposited on the wall η can be estimated by the following expression, which is based on an extrapolation of experiments performed by Samenfink [14] on the interaction of droplets with small waves:

$$\eta_{\text{drywall}} = S^{-0.6} \tag{27}$$

where S needs to be greater than or equal to 1 for the expression to have meaning.

The mechanisms of wall interaction between droplets and a wet wall are basically the same as for a dry wall, the main difference being an additional damping effect, which is a function of film thickness [6,13]

$$\eta_{\text{film}} = 1 - (1 - \eta_{\text{drywall}})\exp[-h_{\text{film}}/D_o] \tag{28}$$

In gas turbine application, impact Reynolds numbers tend to be high. In addition, the following relationship between the Laplace, Reynolds, and Weber numbers is useful in defining splashing interactions for wall temperatures well below the modified Leidenfrost temperature:

$$\mathrm{La} = \frac{\mathrm{Re}_{\mathrm{imp}}^2}{\mathrm{We}} \tag{29}$$

where the Weber number is given by

$$\mathrm{We} = \frac{\rho_i w_{n,i}^2 D_i}{\sigma_i} \tag{30}$$

Hence, whereas low Laplace numbers tend to be associated with droplet splashing, high Weber numbers tend to result in splashing. The following four droplet-wall interaction regimes are defined by Zhluktov et al. [6] for application of wet compression in axial compressors:

1. Sticking regime. Impinging droplets adhere to the surface of the film ($\mathrm{We} < 5$).
2. Rebounding regime. Impinging droplets bounce off the surface of the film ($5 < \mathrm{We} > 10$).
3. Spreading regime. Impinging droplets merge with the liquid film upon contact ($\mathrm{We} > 10$; $S < 1$).
4. Splashing regime. A fraction of the impinging droplets is deposited within the wall; the rest is deflected as secondary droplets ($\mathrm{We} > 10$; $S > 1$).

3.2.3 Size of Secondary Droplets. The average size of a secondary droplet, D_m, due to wall splashing is much smaller compared with the size of an average-size parent droplet, D_o. This leads to a larger aggregate surface area of liquid, which will augment evaporation. The following correlation is obtained from experiments applicable to wet compression in gas turbines [13,14]:

$$D_m = D_o \exp\left[-2 - \frac{D_o}{4066} - 0.05S\right]$$
$$= D_o \exp\left[-2 - \frac{D_o}{4066} - \frac{0.05}{24}\mathrm{Re}_{\mathrm{imp}}^{0.162}\,\mathrm{We}^{0.419}\right] \tag{31}$$

Recently, Wu [15] developed a simple model of secondary droplet formation through backward formalism as follows.

1. Droplet size is estimated by Rayleigh instability theory for jet break-up mechanisms based on the diameter of "fingers" jetting out from the droplet-size concave water sheets, or lamella formed during a splashing impact.
2. "Finger" diameter estimation is based on the conservation of mass and surface energy between the fingers and the lamella.
3. Lamella height estimation is based on the conservation of kinetic and surface tension energies due to the fact that the top edge of the lamella does not break up. Consequently, the surface force will drive the edge to move into the liquid at constant velocity.
4. The velocity of the liquid inside the lamella is based on the conservation of mass and energy during impact of the initial droplet by taking into account the surface tension, and the kinetic and viscous dissipations of energy.

This gives the following expression for the average size of the secondary droplets:

$$D_m = \frac{4.23 D_o}{\mathrm{We}}\left[\left[\sqrt{9 + \frac{2\mathrm{We}^2}{\mathrm{Re}_{\mathrm{imp}}}}\right] + 3\right] \tag{32}$$

The predictions it yields are in agreement with the investigation done by Akhtar and Yule [16], in which droplet impaction on a heated surface at high Weber numbers was investigated.

3.3 Film Evaporation. Hill [1] estimated that most of the evaporation occurring within a compressor with water injection takes place in surface films. He based this conclusion on a water mass flow balance between injected water and residual water, which he collected in bleed cavities and other sources of leakage, along with calculations he made of surface film evaporation rates. Unfortunately, he did not give any details regarding these surface film calculations. That being said, the evaporative-cooling compressor mean-line code calibration studies performed on Alstom industrial gas turbines conclude that the film evaporation effects contribute less than 10% to the total water evaporation with the compressor stages, and do little to lower the temperature of the gas since heat from the metal surfaces primarily drives the evaporation of the surface films.

3.3.1 Estimation of Adiabatic Film Thickness. It is assumed that all liquid on the wall surfaces travels in a flat, thin film. The triangular relationship and interfacial roughness model by Whalley [17] can be used to calculate the thicknesses and velocities of the films on the hub and casing. Such is utilized by Zhluktov et al. [6] in axial compressor application. The liquid flow rate can be found by integrating the velocity profile across the liquid film. Such a model relates three variables: flow rate of liquid film, W_l, film shear stress, τ, and average film thickness, h. The authors of this work contemplate the following algorithm.

1. Calculate the Reynolds number, $\mathrm{Re}_L = L\rho_g u_g / \mu_g$.
2. Calculate the single phase friction factor of the gas, $C_{fg} = f(\mathrm{Re}_L)$.
3. Calculate the interfacial friction factor, $C_{fi} = f(C_{fg}, \varepsilon_i)$.
4. Calculate the film shear stress at the interface, $\tau = \frac{1}{2} C_{fi} \rho_g u_g^2$.
5. Calculate the dimensionless liquid flow rate, $W^+ = W_l / L\mu_l$.
6. Use the expressions of Whalley [17] to find the dimensionless film thickness, $h_i^+ = f(W^+)$.
7. Calculate the film thickness, $h_{i+1} = h_i^+ \mu_l / (\tau\rho_l)^{0.5}$.
8. Estimate the surface roughness, ε_l, from the film thickness, h_{i+1}, according to Whalley [17].
9. Go back to step 3 and iterate, assuming that the film thickness is determined when $|(h_{i+1} - h_i)/h_i| < 10^{-4}$.

3.3.2 Blade, Casing, and Hub Temperatures. The surface temperatures of the blades, casing, and hub need be known in order to account for the effect of film evaporation. It is assumed that the temperature of the wall surface is slightly lower than the total temperature of the gas [6].

3.3.3 Film Evaporation and Heating Rates. Again, Zhluktov et al. [6] formulated an expression for the evaporation rate on a wall surface as follows:

$$\frac{\dot{m}_{\mathrm{wall}}}{A} = (X_{d,\mathrm{surf}} - X_{d,\mathrm{fs}})\frac{\mu_g}{\delta} \tag{33}$$

where $X_{d,\mathrm{surf}}$ is the mass fraction of vapor at the film surface, $X_{d,\mathrm{fs}}$ is the mass fraction of vapor in the freestream, and δ is the boundary layer thickness of the gas above the wetted blade surface. The heating rate can be calculated as follows:

$$\frac{\dot{Q}}{A} = C_{pg}(T_g - T_{\mathrm{surf}})\frac{\mu_g}{\delta} \tag{34}$$

On the blade and vane pressure surfaces he utilized the following correlation:

$$\frac{u_g \mu_g}{\delta} = 0.058\rho_g \frac{u_g^2}{2}\mathrm{Re}_{\mathrm{bld}}^{-0.20} \tag{35}$$

where

$$\mathrm{Re}_{\mathrm{bld}} = \frac{\rho_g u_g \mathrm{chord}/2}{\mu_g} \tag{36}$$

On the hub and casing, he utilized the following:

$$\frac{u_g \mu_g}{\delta} = 0.079\rho_g \frac{u_g^2}{2}\mathrm{Re}_{\mathrm{wall}}^{-0.25} \tag{37}$$

where

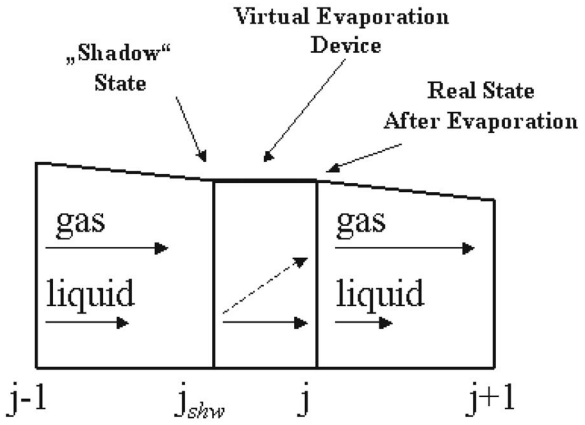

Fig. 6 Schematic of virtual evaporation device

$$\mathrm{Re}_{\mathrm{wall}} = \frac{\rho_g u_g 2(R_{\mathrm{casing}} - R_{\mathrm{hub}})}{\mu_g} \tag{38}$$

Zhluktov et al. [6] also assumed that water not evaporating on blade surfaces is either slung out to the casing as with rotor blades, or flows in equal proportions to both the hub and the casing as with vanes.

4 Aerodynamic Effects

The evaporative-cooling compressor mean-line model contains computing stations at leading and trailing edges of all blades and vanes in the flow path. No intrablade stations are utilized, meaning that airfoil losses and flow-angle deviations are applied at the trailing-edge stations of respective blades and vanes. Likewise, evaporative effects on flow angle are applied at the trailing-edge stations on a row-by-row basis.

4.1 Flow-Angle Correction. In order to apply the effects of evaporation on the compressor blade and vane row trailing-edge stations, a zero-length, constant-area virtual evaporation device is employed within the mean-line code; see Fig. 6. It is within this device that stagewise evaporation takes place under the conditions of constant swirl.

In the virtual evaporation device, the equations of conservation of mass, momentum, and energy for the mixture of water droplets and gas are

$$\dot{m}_1 + \sum \dot{m}_{i,1} = \dot{m}_2 + \sum \dot{m}_{i,2} \tag{39}$$

$$p_1 A + \dot{m}_1 c_{m,1} + \sum \dot{m}_{i,1} c_{m,1} = p_2 A + \dot{m}_2 c_{m,2} + \sum \dot{m}_{i,2} c_{m,2} \tag{40}$$

and

$$\dot{m}_1\left(h_1 + \frac{c_{m,1}^2}{2} + \frac{c_{u,1}^2}{2}\right) + \sum \dot{m}_{i,1}\left(h_{i,1} + \frac{c_{m,i,1}^2}{2} + \frac{c_{u,i,1}^2}{2}\right) = \dot{m}_2\left(h_2 \frac{c_{m,2}^2}{2} + \frac{c_{u,2}^2}{2}\right) + \sum \dot{m}_{i,2}\left(h_{i,2} + \frac{c_{m,i,2}^2}{2} + \frac{c_{u,i,2}^2}{2}\right) \tag{41}$$

where the subscripts 1 and 2 denote the respective inlet and outlet stations of the virtual evaporation device. The contributions of the droplet classes i sum up to the total mass, momentum, and energy of the liquid phase. The left hand sides of the above conservation equations, known as the shadow state, are known from the standard mean-line calculation. The state of the liquid at station 2, the exit of the virtual evaporation device, is known from the integration of the aforementioned droplet equations. With the assumption of the swirl at the exit station of a blade or vane row being unaffected by evaporation, $c_{u,1} = c_{u,2}$, and the equation of state, the unknown values of pressure, enthalpy, density, and velocity at the real state after evaporation, station 2, may be calculated.

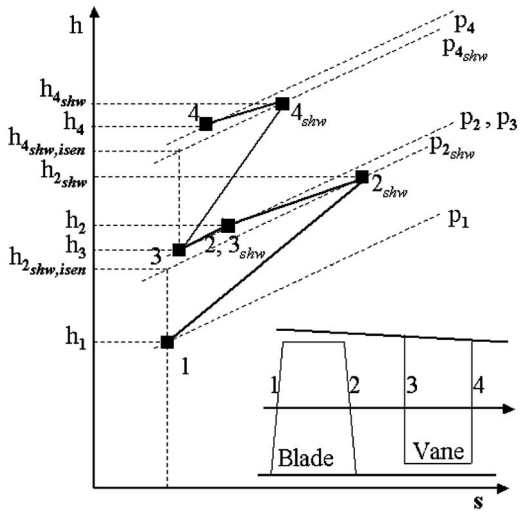

Fig. 7 *h-s* diagram detailing entropy decreases from evaporation

Typically, the gas velocity decreases a few percent in the virtual evaporation device due to cooling. Consequently, at the blade and vane trailing edges, where the respective relative and absolute flow angles are specified (see station j_{shw} in Fig. 6), a slightly different flow angle at position j results due to the assumption of constant swirl. To determine the specified flow angle at a stator trailing edge, the tangential velocity $c_{u,2}$ is corrected at position j based on the meridional velocity $c_{m,2}$ as follows:

$$\frac{c_{u,2}}{c_{m,2}} = \frac{c_{u,1}}{c_{m,1}} \tag{42}$$

At a rotor trailing edge, the tangential velocity $c_{u,2}$ is corrected to determine the specified relative flow angle

$$\frac{w_{u,2}}{c_{m,2}} = \frac{w_{u,1}}{c_{m,1}} \tag{43}$$

where

$$c_{u,2} = w_{u,2} + \omega R \tag{44}$$

The corrections in c_u are small; therefore, corrected values are used to correct the right-hand side of the steady-state–steady flow energy equation.

4.2 Aerodynamic Efficiency. Although relatively small for any particular stage, trailing-edge flow-angle correction for evaporation has a compounding effect on a multistage compressor. Hence, an additional polytropic efficiency calculation was put into the mean-line code in order to separate evaporative effects from the aerodynamic effects of stage rematching; see Fig. 7. Basically, by subtracting out the effects of decreases in entropy due to cooling, it is possible to calculate a stage efficiency reflecting the rematching

$$\eta_{\mathrm{isen}} = \frac{(h_{2_{\mathrm{shw,isen}}} - h_1 + h_{3_{\mathrm{shw,isen}}} - h_2 + h_{4_{\mathrm{shw,isen}}} - h_3)}{(h_{2_{\mathrm{shw}}} - h_1 + h_{3_{\mathrm{shw}}} - h_2 + h_{4_{\mathrm{shw}}} - h_3)} \tag{45}$$

4.3 Aerodynamic Loading Description of Hill. Prior to the first compressor water injection test at Alstom, it was assumed that the compressor air mass flow would increase, as reported by Hill and others. That is, the rear stages would load up aerodynamically, sucking down on the front stages in the process. For back stages to load up aerodynamically, the meridional flow vectors must shorten despite the creation of gas from evaporation. Thus,

the increase in the density of the gas from cooling needs to dominate. In the front stages, where little evaporation takes place, it was assumed that a lengthening of the meridional flow vector would occur mainly due to increased air mass flow as these stages are pulled down on their characteristics. Following the testing of Alstom industrial compressors, such turned out to not always be the case. That is, at operating conditions far below design, where back-stage incidences move far in the choked direction, one could observe that air mass flow increases proportional to flow rate of water injected. However, near design operating conditions, air mass flow was observed to fall-off with increasing mass flow under the conditions of ambient relative humidity near 100%, while behaving like a Hill compressor [1] at lower levels of humidity.

4.4 Wetted-Surface Flow Deviation Effect. The work of Day et al. [9] provides a description of the effects of water injection into compressor stages, which can be referred to in explaining why compressor mass flow might drop off with injection, the aforementioned effects of rearward aerodynamic load shift notwithstanding. In experiments, they demonstrated that when large amounts of water are injected into a compressor stage, most ends up being slung radially into the outer spans, causing air flow to be pushed toward the root region. The tip region, in effect, operates more stalled since it is robbed of flow. Moreover, cascade angle measurements indicated that trailing-edge relative flow-angle deviation increased in the tip regions of rotor blade cascades and fell off in the root regions. Although they did not report the overall effect on air flow for a wet cascade, it seems reasonable that the tip region should dominate, and that the overall effect should be a reduction in air mass flow for the cascade.

It should be pointed out that the cascade tests done by Day et al. [9] involved large levels of water injection—17% of inlet mass flow and higher—in comparison to levels normally injected into industrial compressors for purposes of power augmentation. For that matter, They were mainly interested in the effects of aircraft compressors on runway approach during heavy rainstorms. Hence, it is reasonable to assume that at much lower levels of injection typical of application in industrial gas turbines, the radial shift in airflow reported in the investigation of Day et al. [9] would not be so pronounced, and that in many instances compressors with water injection would behave as they do in the Hill investigation [1]; i.e., mass flow would increase.

What the investigation of Day et al. [9] does make apparent for industrial compressor application is the fact that one needs to account for some degree of aerodynamic degradation of compressor performance due to the wetting of the blades from the ingestion of water. Calibration of a compressor mean-line code for the effects of wetted blades does not allow for the input of radial distributions of flow-angle deviation adders. In fact, the cascade tests of Day et al. [9] indicate that no change in cascade flow-angle deviation occurs near the RMS span. Nonetheless, if one is to take such effects into account when calibrating a mean-line code, then one has no choice but to apply deviation adders there.

A wetted-surface flow-angle deviation adder was therefore considered for the evaporative-cooling compressor mean-line calibration for Alstom gas turbines. Since it was realized that the dominant influence on compressor mass flow is the first rotor blade, no attempt was made to distribute deviation across all of the wetted stages, not that one would know how to do so if one wished to do so.

5 Boundary Conditions for Calculation

An overview of the setup for calculations with the evaporative-cooling compressor mean-line code is given in Fig. 8. In all applications of Alstom gas turbines, a rack of water injection nozzles is situated on top of the intake manifold. At this location the flow is of the order of 20 m/s, a low enough level for the flow to be in thermodynamic equilibrium. Boundary conditions to the code include the flow conditions at the injection plane—temperature, pressure, humidity, water mass flow rate and water temperature—as well as compressor speed and vane positions, the compressor exit pressure set by the turbine, and the flow rates of all intracompressor extractions. The output from the calculation includes changes in compressor mass flow, efficiency, and power consumption, wet to dry, as well as changes in bleed supply pressure and temperatures at the compressor exit and at the bleeds.

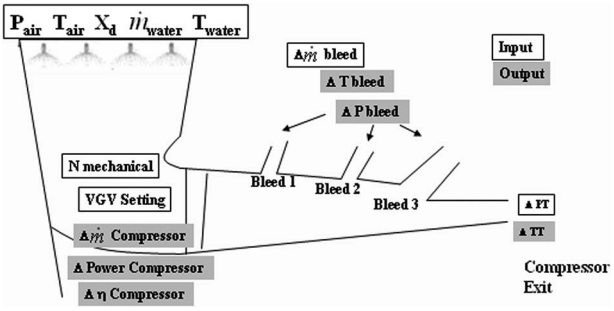

Fig. 8 Schematic of mean-line boundary conditions

An additional boundary condition is the water injection nozzle spectrum, as measured by Malvern spectral analysis equipment in an intake facility featuring length dimensions typical of an Alstom gas turbine. As input for the mean-line code, the measured spectra were approximated by the Sauter mean diameter, which relates volume to surface area

$$D_{32} = \sum_{i=1}^{N} D_i^3 / \sum_{i=1}^{N} D_i^2 \tag{46}$$

6 Details of the Calibration Data Analysis

Water injection tests of industrial gas turbines operating at constant speeds of either 50 Hz or 60 Hz require relatively constant ambient conditions over a period of 3–4 h, assuming the unit has already had sufficient time to reach thermal equilibrium. Under such conditions it is possible to generate heat balances of the gas turbine in a manner described by Cataldi et al. [18]. In fact, since they worked with the same data sets analyzed in this work, some of their heat balance results are presented as comparisons; see Figs. 9 and 16.

The first steady-state data point of a water injection test is a dry baseline point, followed approximately 1 h later by a data point at the maximum water injection flow rate to be tested. In this way, the two most essential data points are obtained within 1 h, meaning the test would still be worthwhile should ambient conditions then suddenly change. Additional data points are then obtained, weather permitting, at lower levels of water injection.

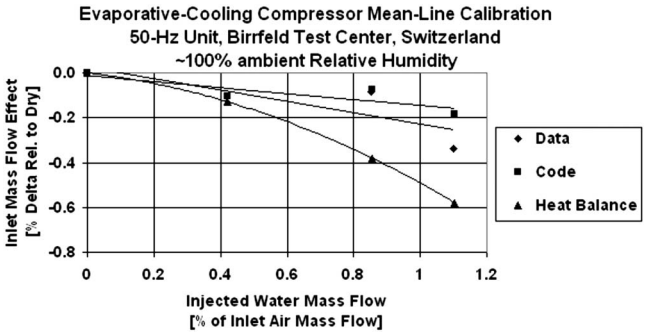

Fig. 9 Modeling of mass flow at 100% ambient relative humidity

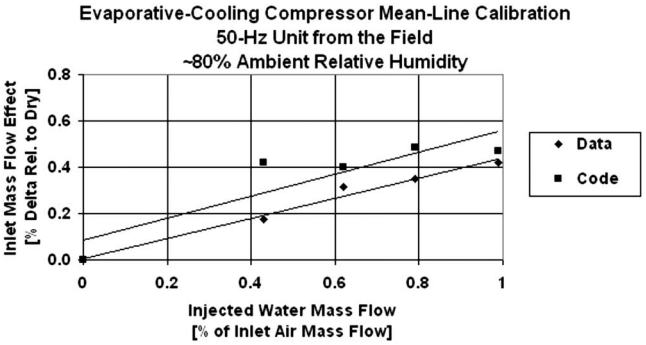

Fig. 10 Modeling of mass flow at 80% ambient relative humidity

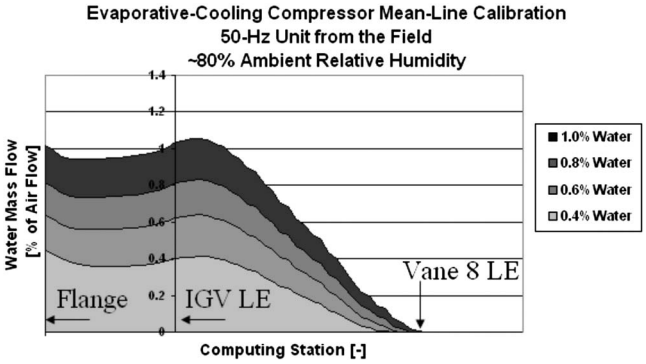

Fig. 12 Compressor axial water distribution at 80% ambient relative humidity

6.1 Calibration Data Set. Of the two 50 Hz tests involving different compressor models of the same GT family, which were performed in Alstom's Switzerland Test Center, the weather only remained cooperative for one. Ambient conditions during that test were approximately 10°C and 100% relative humidity. Subsequent tests at customer sites were performed on 50 Hz and 60 Hz units of like-family compressors as were tested in Switzerland. Although the ambient conditions remained relatively constant for both tests, only the 50 Hz unit was equipped with static pressure taps in the intake bell mouth, meaning that mass flow effects with water injection could not be directly investigated on the 60 Hz unit. During the test on the 50 Hz unit, the ambient temperature was approximately 18°C and the relative humidity, about 80%. Moreover, this test involved the same compressor model as in the successful 50 Hz test in Switzerland.

6.1.1 Inlet Mass Flow. A linear function of wetted-surface flow-angle deviation adder with water injection rate was required to match the two data sets at 80% and 100% relative humidities. Figures 9 and 10 contain compressor inlet mass flow versus water injection level for the 100% and 80% relative humidity data sets, respectively. Note that the lower humidity data set seems to behave like a Hill compressor [1] in the sense that any wetted-surface flow-angle deviation effect is masked by suck-down, as indicated by air mass flow rate increasing with water injection level. However, at 100% relative humidity, the mass flow drops off with water injection, leading one to formulate the contradictory hypothesis, mainly that wetted surfaces have an effect significant enough to be noticed.

A detailed explanation as to how mass flow can increase or decrease with water injection in identical compressor models is found in Figs. 11 and 12. These figures contain station-by-station distributions of water flow rate starting at the injection flange located above the manifold, and progressing into the compressor until completely evaporating by stage 8 or thereabouts. Note that for 80% ambient relative humidity the code predicts some degree of evaporation taking place in the intake manifold, followed by condensation as the static pressure rapidly falls off in the bell mouth as the compressor face is reached. For that matter, the flow rate of water at compressor blade one leading edge is about equal to the level injected at the flange; contrast this effect with that of the calculations at 100% ambient relative humidity. In this case there is some small degree of condensation taking place in the intake manifold, followed by additional condensation in the intake bell mouth leading up to the compressor face. Unlike at the lower humidity level, in this instance the water flow rate at compressor blade one leading edge is actually greater than the level injected, thus, providing for the basis of explanation for the air mass flow dropping off at the higher humidity level. That is, relative to the data set taken at 80% relative humidity, the higher water mass flow at the leading edge of the blade due to increased condensation under conditions of 100% ambient relative humidity warranted the input of about 0.2 deg more blade trailing-edge flow-angle deviation in the mean-line model at maximum water injection, which resulted in the matching of mass flows from both data sets as indicated in Figs. 9 and 10.

6.1.2 Bleed Supply Pressure Effects. The degree to which the evaporative-cooling compressor mean-line code matches bleed supply pressure suck-down effects is shown in Figs. 13 and 14 for the cases of 100% and 80% ambient relative humidities, respectively. The exit pressure of the compressor rises with increasing water injection flow rates because the gas turbine is run to constant turbine inlet temperature. Hence, as more water is injected, and the compressor exit temperature decreases more, the turbine output increases, and higher compressor operating lines are set.

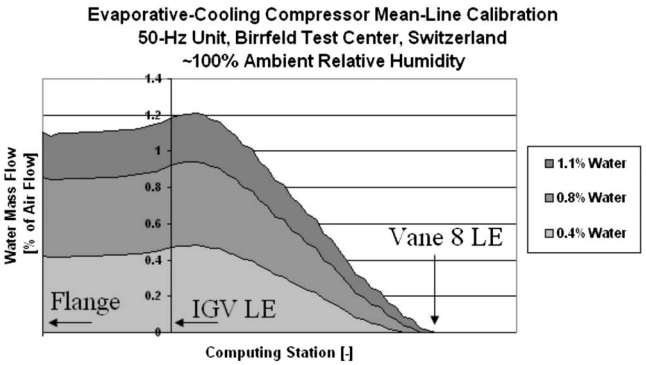

Fig. 11 Compressor axial water distribution at 100% ambient relative humidity

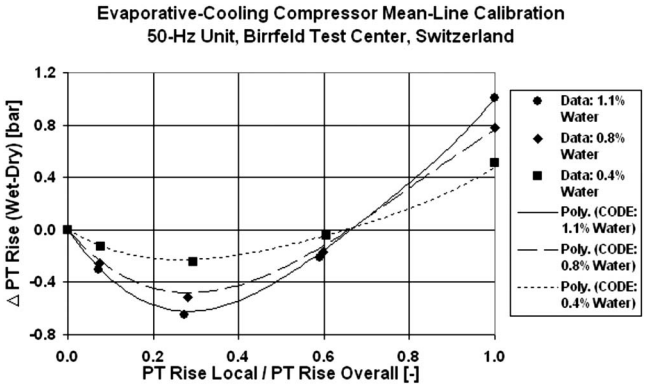

Fig. 13 Modeling of bleed supply pressure at 100% ambient relative humidity

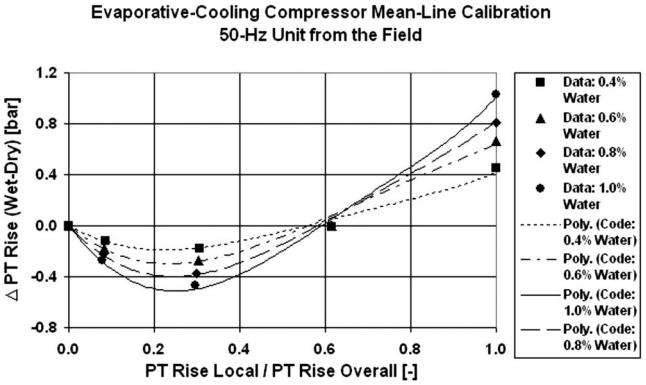

Fig. 14 Modeling of bleed supply pressure at 80% ambient relative humidity

Also of note is the fact that the bleed supply pressure suck-down of the third bleed corresponding to the unit operating at 80% humidity is approximately zero, whereas about 250 mbars of suck-down can be seen in the data taken on the unit running at 100% humidity. This effect has nothing to do with the humidity level. Rather, the unit running at 80% humidity had a differently sized orifice installed in this bleed line, which changed the boundary conditions to the compressor.

6.1.3 Bleed Cool-Down Effects. Modeling bleed-cavity cool-down effects with the mean-line code proved to be more challenging than modeling suck-down effects. For one, the bleed located just behind the fifth stage on all units extracts an air-water mixture. In addition, it was not known to what extent radial slinging of water would affect the composition of this air-water mixture. Luckily, colleagues monitoring the lifetime of components cooled by intracompressor bleed flows were more interested in the mass flow levels of cooling air than they were interested in the temperatures of these cooling flows. Thus, attention was focused on predicting the bleed suck-down effects.

One can get a reasonable estimate of bleed-cavity cool-down with water injection by using measured vane leading-edge total temperature profiles obtained during dry operation, or even wet operation if located deep enough the compressor as to not get wet; see Fig. 15. For various levels of water injection, one superimposes temperature profile data onto mean-line calculations to obtain reasonable levels of cool-down.

6.1.4 Compressor Power Consumption. Thermodynamic calculations can be made on these wet-compression data sets to confirm that compressor power consumption should fall-off with water injection due to an effect similar to intercooling. It is important to point out, however, that the Alstom gas turbines tested were

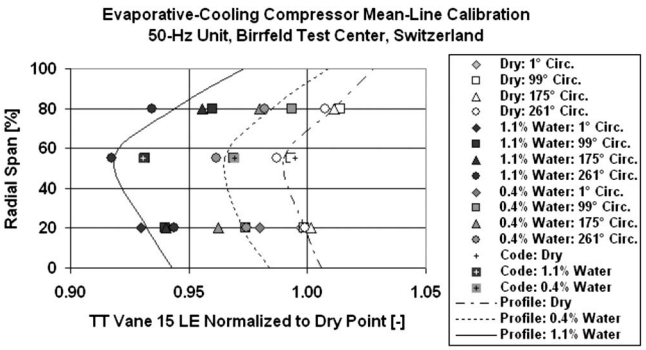

Fig. 15 Interstage temperature data utilized to predict bleed-cavity cool-down effects

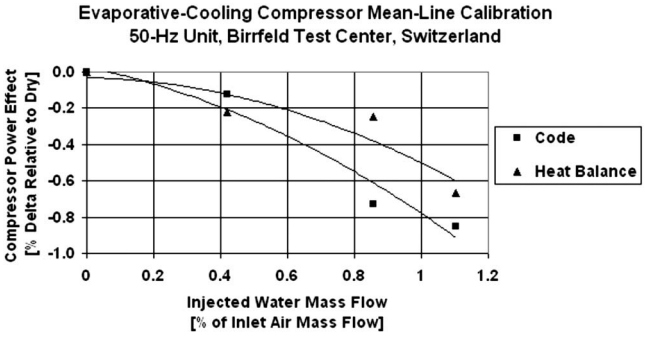

Fig. 16 Compressor power consumption comparison

operated at constant turbine inlet temperature, meaning that turbine output was increased, and compressor exit pressure was increased. That being said, the mean-line models of the data sets of the two Alstom 50 Hz compressors tested did indicate power consumption fall-off with water injection. See Fig. 16 for a comparison of the power calculations from calibrated mean-line and the heat balance method of Cataldi et al. [18] made on the Birrfeld data set.

6.2 Water Penetration Check on the Model. With the accrual of wet-compression operating hours in the field, an opportunity arose in which the evaporative-compressor cooling mean-line could be checked for its ability to predict how deep injected water penetrates into a compressor before evaporating. The machine involved was a 60 Hz field unit in North America. Following considerable operating hours of base-load wet compression at 1% of inlet mass flow, the unit underwent a scheduled maintenance outage, at which time inspectors observed evidence of stagewise water penetration. They reported the presence of water stains on the leading edges of the rotor blades as deep as row 8, which is precisely the row in which water completely evaporates in the mean-line model; see Figs. 17–20.

7 Conclusion

A compressor mean-line tool has been calibrated to predict wet-compression effects in industrial axial compressors with water injection levels of the order of 1% of inlet air mass flow. During the effort, it was discovered that stagewise evaporation rates strongly affect the compressor interstage bleed supply pressures. Modeling these effects reasonably well for the levels of water injection studied required the acceleration of evaporation above what would be predicted by a single-droplet evaporation model. For that matter, taking into account the additional effects of drop-

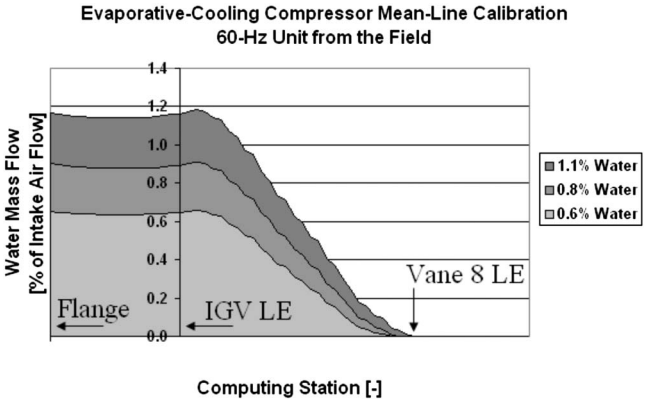

Fig. 17 Compressor axial water distribution on a 60 Hz field unit

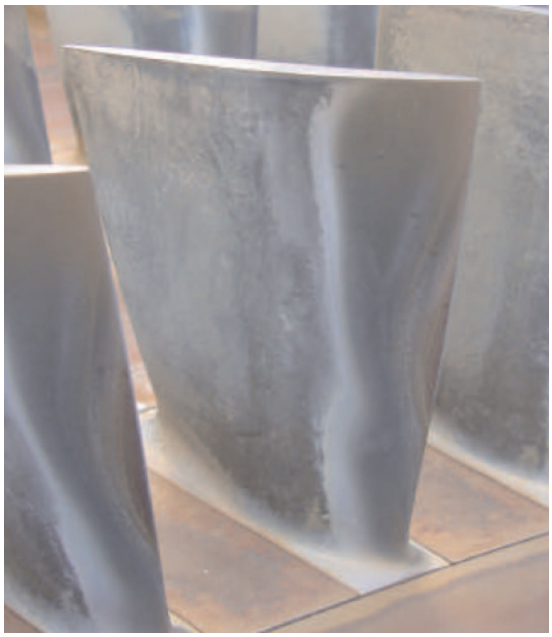

Fig. 18 Appreciable water stain on the suction side of blade row 7 of a 60 Hz unit

let splashing and surface film formation was required. In order to model compressor mass flow effects with water injection, a simple airfoil flow-angle deviation adder was applied to the first compressor blade as a linear function of water injection rate modified by any evaporation or condensation taking place in the intake manifold leading up to the leading edge of this blade. The model was successfully applied to two 50 Hz Alstom units of identical compressor model operating under ambient relative humidity levels of 80% and 100%. From these tests it was concluded that water injection into an axial compressor involves the counterbalancing of an aerodynamic shifting of load to the rear stages—and corresponding unloading of front stages along with increased air mass flow—against the tendency for wetted blades of front compressor stages to be less capable of performing work.

Fig. 19 Water stain on the suction side of blade row 8 of a 60 Hz unit

Fig. 20 Absence of water stains on blade row 9 of a 60 Hz unit

Acknowledgment

We wish to thank all the people whose efforts were necessary for the development of this mean-line code, including Werner Schmidhofer and those at the Alstom Test Center in Birrfeld, Switzerland, the commissioning crews in the field, and Juergen Hoffmann and the project team at Alstom. We certainly could never have embarked on this research without their steadfast commitment to making these water injection tests happen. We would also like to thank engineer Gustov Hagstroem, who took the photographs of the blade leading-edge water stains while on site.

Nomenclature

Γ = diffusion coefficient (mm^2/s)
λ = thermal conductivity (W/m K)
L = specific enthalpy of evaporation (kJ/kg)
c_D = drag coefficient
μ = dynamic viscosity (Pa s)
c_p = specific heat at constant pressure (kJ/kg K)
P = pressure (Pa)
T = temperature (K)
ρ = density (kg/m^3)
t = time coordinate (s)
D = droplet diameter (μm)
Re = Reynolds number
Nu = Nusselt number
Sc = Schmidt number
Pr = Prandtl number
s = meridional coordinate (mm)
$\dot{n}$ = droplet flow rate (droplet/s)
$\dot{m}$ = mass flow rate (kg/s)
$\dot{Q}$ = heat transfer rate (kJ/s)
ε = emissivity

σ = Stefan–Boltzmann constant ($W/m^2 K^4$)
l = length (mm)
b = axial length (mm)
d = cascade pitch (mm)
β = relative trajectory angle (air or droplet) (deg)
c = absolute velocity (m/s)
w = relative velocity (m/s)
U = wheel speed (m/s)
n_b = number of blades
N = number of droplets
$\dot{N}$ = droplet impact rate (droplet/s)
f = droplet impact frequency (1/s)
ω = angular speed (1/s)
R = radial dimension (mm)
We = Weber number
La = Laplace number
η = fraction of deposited droplets
h = film thickness (mm)
σ = surface tension (Nt/m)
u = velocity (m/s)
C_f = coefficient of friction
ε = surface roughness (μm)
τ = film shear stress (Nt/mm^2)
W_l = film flow rate (ml/s)
X_d = mass fraction of vapor
δ = boundary layer thickness (mm)
A = area (mm^2)
η = efficiency
h = specific enthalpy (kJ/kg)
s = specific entropy (kJ/kg K)

Subscripts

i = droplet class, interfacial, initial quantity
s = saturated state, Sauter mean
m = meridional component, mean quantity
u = tangential component
l = liquid phase
wet = droplet-impacted
v = vapor phase
g = gaseous phase (air plus vapor)
rad = radiation
conv = convection
n = normal component
imp = impact
o = initial or parent quantity
film = water film
L = length
wall = wall
bld = blade
surf = film surface
fs = freestream
shw = shadow
isen = isentropic
32 = Sauter mean

References

[1] Hill, P. G., 1963, "Aerodynamic and Thermodynamic Effects of Coolant Injection on Axial Compressors," Aeronaut. Q., **February**, pp. 331–348.
[2] Tsuchiya, T., and Murthy, S. N. B., 1982, "Water Injection Into Axial Compressors," AIAA Paper No. 82-0196.
[3] Utamura, M., Kuwahra, T., Murata, H., and Horii, N., 1999, "Effects of Intensive Evaporative Cooling on Performance Characteristics of Land-Based Gas Turbine," Joint Power General Conference, Vol. PWR-34/2, ASME, New York, pp. 321–328.
[4] Horlock, J. H., 2001, "Compressor Performance With Water Injection," ASME Paper No. GT-2001-0343.
[5] Camp, T. R., and Horlock, J. H., 1994, "An Analytical Model of Axial Compressor Off-Design Performance," ASME J. Turbomach., **116**, pp. 425–434.
[6] Zhluktov, S. V., Bram, S., and De Ruyck, J., 2001, "Injection of Water Droplets in Axial Compressor," *Proceedings of the Fifth World Conference in Experimental Heat Transfer, Fluid Mechanics, and Thermodynamics*, Thessaloniki, Greece, pp. 1415–1420.
[7] White, A. J., and Meacock, A. J., 2003, "An Evaluation of the Effects of Water Injection on Compressor Performance," ASME Paper No. GT-2003-38237.
[8] van Liere, J., Meijer, C. G., Laagland, G. H. M., and Anemaat, C. A., 2000, "Swirlflash: One Year On," Mod. Power Syst., **April**, pp. 26–27.
[9] Day, I., Williams, J., and Freeman, C., 2005, "Rain Ingestion in Axial Flow Compressors at Part Speed," ASME Paper No. 2005-GT-68582.
[10] Meacock, A. J., and White, A. J., 2006, "The Effect of Water Injection on Multispool Gas Turbine Behavior," ASME J. Eng. Gas Turbines Power, **128**, pp. 97–102.
[11] Young, J. B., 1995, "The Fundamental Equations of Gas-Droplet Multiphase flow," Int. J. Multiphase Flow, **21**, pp. 175–191.
[12] Kobayasi, K., 1954, "The Evaporation Velocity of Single Droplets of Liquid," Engineers Digest, **15**, pp. 463–465.
[13] Schmehl, R., Rosskamp, H., Willmann, S., and Wittig, S., 1999, "CFD Analysis of Spray Propagation and Evaporation Including Wall Film Formation and Spray-Film Interactions," Int. J. Heat Fluid Flow, **20**, pp. 520–529.
[14] Samenfink, W., 1997 "Grundlegende Untersuchung zur Tropfeninteraktion mit Schubspannungsgetriebenen Wandfilmen," Ph.D. thesis, Institut für Thermische Strömungsmschinen, Universität von Karlsruhe, Karlsruhe, Germany.
[15] Wu, Z., 2003, "Backward Formalism to Derive the Size of Secondary Ejected Droplets Produced by Crown Splashing of Drops Impinging on a Solid Wall," Commun. Math. Sci., **1**, pp. 57–67.
[16] Akhtar, S. W., and Yule, A. J., 2001, "Droplet Interaction on a Heated Surface at High Weber Numbers," *Proceedings of ILASS-Europe*, Zürich, pp. 718–723.
[17] Whalley, P. B., 1987, *Boiling, Condensation and Gas-Liquid Flow*, Clarendon, Oxford.
[18] Cataldi, G., Güntner, H., Matz, C., McKay, T., Hoffmann, J., Nemet, A., Lecheler, S., and Braun, J., 2006, "Influence of High Fogging Systems on Gas Turbine Operation and Performance," ASME J. Eng. Gas Turbines Power, **128**, pp. 135–143.